Seismic imaging and illumination with internal multiples

Alison E. Malcolm,[1] Bjørn Ursin[2] and Maarten V. de Hoop[3]

[1]*Department of Earth, Atmospheric and Planetary Sciences, Massachusetts Institute of Technology, Cambridge, MA, USA. E-mail: amalcolm@mit.edu*
[2]*Norwegian University of Science and Technology (NTNU), Department of Petroleum Engineering and Applied Geophysics, S. P Andersensvei 15A, NO-7491 Trondheim, Norway*
[3]*Center for Computational and Applied Mathematics and Geo-Mathematical Imaging Group, Purdue University, West Lafayette, IN, USA*

SUMMARY

If singly scattered seismic waves illuminate the entirety of a subsurface structure of interest, standard methods can be applied to image it. It is generally the case, however, that with a combination of restricted acquisition geometry and imperfect velocity models, it is not possible to illuminate all structures with only singly scattered waves. We present an approach to use multiply scattered waves to illuminate structures not sensed by singly scattered waves. It can be viewed as a refinement of past work in which a method to predict artefacts in imaging with multiply scattered waves was developed. We propose an algorithm and carry out numerical experiments, representative of imaging of the bottom and flanks of salt, demonstrating the effectiveness of our approach.

Key words: Computational seismology; Theoretical seismology; Wave scattering and diffraction.

1 INTRODUCTION

Imaging with multiples was first proposed in a Kirchoff framework for water column multiples in Reiter *et al.* (1991). In recent years imaging with surface-related multiples has garnered a great deal of attention (Guitton 2002; Berkhout & Verschuur 2006; Muijs *et al.* 2007a,b). In these methods, primaries are used as a source function for imaging with surface-related multiples directly. As was done in Malcolm *et al.* (2007) to estimate image artefacts, these techniques could be extended to apply to internal multiples by performing similar procedures at depth. Through interferometric imaging, in particular for VSP data, additional work has been done on imaging with multiples. An overview of this work is given in Schuster *et al.* (2004) and Jiang *et al.* (2007); in this case the multiples are turned into primaries through interferometry and then standard migration techniques are applied. Several other examples exploiting these ideas are given in Jiang (2006) and Vasconcelos *et al.* (2007). To our knowledge this is the first demonstration of direct imaging of the underside of a complicated geologic structure using surface data. The work of Youn & Zhou (2001) could certainly generate similar results, but their method is significantly more computationally intensive and requires prior knowledge of the location of the deeper reflector in multiple generation, which our method does not.

In this paper, we introduce a method of including multiply scattered waves in one-way wave equation based migration. The method has the potential to improve, in particular, images of the base of salt and of near-vertical structures such as salt flanks or faults. Our approach extends the work of Malcolm & de Hoop (2005) by including illumination in a series representation that models the data as a superposition of different phases. By explicitly including illumination in the series we identify those multiples which carry information about regions of the subsurface not illuminated by singly scattered waves.

Imaging with multiply scattered waves based on a one-way wave equation, requires a 'multipass' approach reminiscent of the generalized Bremmer series (de Hoop 1996). Turning waves can, in principle, also be accounted for in such an approach (Xu & Jin 2006; Zhang *et al.* 2006; see also Hale *et al.* 1991). In the multipass approach, starting at the surface (or top), waves are first propagated downwards and then stored at each depth; in the second 'pass', starting at the bottom, reflection operators derived from the image (formed in the first pass) are applied to the stored fields and the results are propagated, accumulatively, back upwards. With each pass an additional scatter is incorporated on both the source and receiver side. Although turning waves could be incorporated in such a framework, they can be incorporated in the one-way wave equation more naturally by introducing proper curvilinear coordinates (and the associated Riemannian metric Stolk & de Hoop 2007).

The approach proposed in this paper integrates elements of Jin *et al.* (2006) and Xu & Jin (2007), who developed a way to image near-vertical structures with doubly scattered waves, with Malcolm & de Hoop (2005), who developed the inverse generalized Bremmer coupling series. Here, we modify this series to incorporate illumination effects to arrive at a method to generate partial images with different orders of multiply scattered waves. The final image is then constructed from these partial images (*cf.* Fig. 1). The inverse generalized Bremmer
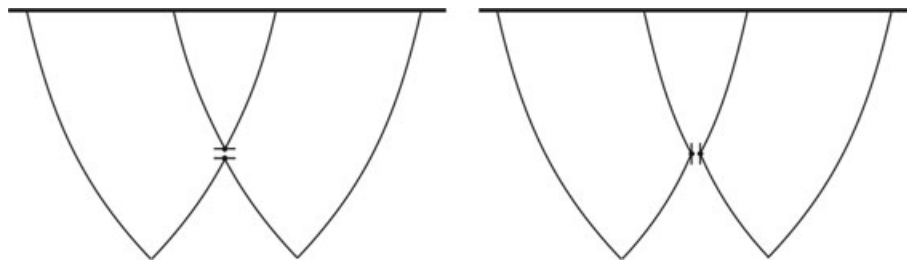
Figure 1. Assimilation of partial images. Examples of 'topside' reflection (singly scattered waves, left-hand side), 'underside' reflection (triply scattered waves, left-hand side) and 'prismatic' reflections (doubly scattered waves, right-hand side) considered in this paper. The deep reflector (not drawn) will be assumed to appear in the image of the first pass.

coupling series combines aspects of the Lippmann–Schwinger equation driven inverse scattering series developed by Weglein *et al.* (1997, 2003) with the generalization of the Bremmer series (Bremmer 1951) developed by de Hoop (1996). Standard migration techniques typically take into account only the first term of these respective series, which is the single scattering assumption ubiquitous in seismic imaging. Our general interest is imaging with 'underside' reflections; the numerical results shown in this paper focus on internal multiples.

A method for imaging with surface-related multiples (primarily triply scattered waves) has been proposed by Berkhout & Vershuur (1994) and Berkhout & Verschuur (2006). They transform surface-related multiples into primaries with the 'sources' at the surface reflection points; this approach is expanded upon by Guitton (2002). Elastic-wave surface reflections were also used by Bostock *et al.* (2001) but then in the setting of teleseismic waves and passive sources. Exploiting the information in internal multiples, as is done here, has not been investigated to the same extent, although Jiang (2006) and Vasconcelos *et al.* (2007) show examples using seismic interferometry in which internal multiples are converted into primaries with a different acquisition geometry and then used in standard imaging techniques. Further details on interferometric imaging particularly focusing on the inclusion of surface-related multiples in imaging are found in, for example, Schuster *et al.* (2004) and Jiang *et al.* (2007). On a global scale, Revenaugh & Jordan (1991) have used information contained in reverberations between discontinuities in the mantle to further constrain these discontinuities, through a 1-D inversion procedure.

Although we focus primarily on triply scattered waves, doubly scattered waves are also included in our theoretical framework. These waves have been utilized in the context of imaging near-vertical structures. They are referred to as 'duplex', or 'prismatic' waves, and were first discussed by Bell (1991), directly followed by Hawkins (1994), who discussed their influence on dip moveout (DMO) algorithms. Prismatic reflections have been exploited in a ray-theoretical framework, also in the context of traveltime tomography, by several authors (Bell 1991; Broto & Lailly 2001; Cavalca & Lailly 2005; Marmalyevskyy *et al.* 2005; Cavalca & Lailly 2007). Bell (1991) describes a method by which the location of a vertical reflector is optimized by reducing the traveltime of the doubly scattered waves to an equivalent primary reflection. Marmalyevskyy *et al.* (2005) uses a Kirchhoff method to carry out the imaging in which a near-horizontal reflector is picked and the reflection off this interface is included in the Green's function used in Kirchhoff migration. A mathematical analysis of imaging with doubly scattered waves, related to the approach of Marmalyevskyy, has been carried out by Nolan *et al.* (2006) for a radar problem; a discussion of improvements in illumination for the radar problem is given by Cheney & Bonneau (2004). In Broto & Lailly (2001), Cavalca & Lailly (2005) and Cavalca & Lailly (2007) the authors use the picked traveltimes of doubly scattered waves as part of a traveltime tomography procedure. The goal of their work is to provide an inversion framework that accounts for regions where the forward map for (modelling of) a particular event is 'undefined'. They choose the exploitation of doubly scattered waves as these waves are often recorded at only a subset of the receivers. In this case, primaries and doubly scattered waves are used in a joint inversion for both the velocity model and reflector locations; the doubly scattered waves are included by first identifying them as doubly scattered waves and then minimizing a traveltime misfit between the computed (via ray tracing) and true traveltimes.

Our approach requires neither the explicit identification of multiply scattered waves nor the manual location of near-horizontal reflectors. [Including certain reflectors in the velocity model in reverse-time migration to incorporate multiple scattering has been considered by Mittet (2006); similar ideas are suggested by Youn & Zhou (2001).]

Brown & Guitton (2005) employ a forward scattering series to model the data in a least-squares fitting strategy. Each (surface-related) multiple is assigned to its own contrast function (image). They separate source- and receiver-side multiples. Regularization operators are incorporated to suppress cross talk between the different contrast functions during the least-squares inversion; these operators are designed to boost the cross talk and are added as a penalty term so that the resulting optimization promotes solutions with minimal cross talk. One regularization operator example is the annihilator of Stolk & de Hoop (2006) applied in the image-gather domain to the outcome of the wave-equation angle transform. In our approach we rely on the range of the single scattering operator, which can be characterized by annihilators of the data (de Hoop & Uhlmann 2006). Brown and Guitton also consider a regularization operator that extracts the cross talk by applying the imaging operator for a particular multiple to an estimate of a different multiple the estimate of which is determined by modelling data from the contrast functions (in the current iteration) with the associated multiple scattering operator. Our subtraction procedure is reminiscent of this design, except that it is carried out in the data domain rather than the image domain. This procedure is computationally intensive, however, and so we approximate it with particular pseudo-differential cut-offs tied to the imaging conditions associated with doubly, triply,

etc., scattered waves, to implement our approach. These are reminiscent of the imaging condition used in reverse-time migration (Biondi & Shan 2002; Xie & Wu 2006), derived from directional wavefield decomposition.

The paper is organized as follows. We first review the basic structure of multiple scattering operators in the context of inverse scattering. We then introduce the notion of illumination decomposition. In Section 3, we discuss the formation of images with multiply scattered waves, making use of the illumination decomposition, and propose a corresponding algorithm. We carry out numerical experiments demonstrating the effectiveness of our approach in Section 4.

2 MULTIPLE SCATTERING: IMAGE ARTEFACTS AND ILLUMINATION

2.1 Directional decomposition

We consider acoustic wave propagation, governed by the system of equations

$$\partial_z \begin{pmatrix} u \\ \partial_z u \end{pmatrix} = \begin{pmatrix} 0 & 1 \\ -A & 0 \end{pmatrix} \begin{pmatrix} u \\ \partial_z u \end{pmatrix} + \begin{pmatrix} 0 \\ -f \end{pmatrix}, \tag{1}$$

where

$$A = A(z, x, \partial_x, \partial_t) = \partial_x^2 - c(z, x)^{-2} \partial_t^2, \tag{2}$$

where u is the particle displacement, and f is the source density of injection rate; x denotes the 'horizontal' coordinates, t is time and z is the 'depth' coordinate. The velocity c is assumed to be a smooth function. In n-dimensional seismics, $x = (x_1, \ldots, x_{n-1})$, $n = 2, 3$. To facilitate the decomposition of the wavefield into constituents that have been scattered a specific number of times, we split the wavefield into up- and downgoing components, as in the development of the Bremmer series decomposition (de Hoop 1996); the analysis can be found in Stolk & de Hoop (2006). We introduce a z-family of decomposition operators, $\mathbf{Q}(z)$, with

$$U := \begin{pmatrix} u_+ \\ u_- \end{pmatrix} = \mathbf{Q}(z) \begin{pmatrix} u \\ \partial_z u \end{pmatrix}, \qquad \begin{pmatrix} f_+ \\ f_- \end{pmatrix} = \mathbf{Q}(z) \begin{pmatrix} 0 \\ -f \end{pmatrix}, \tag{3}$$

that diagonalize system (1) according to

$$\mathbf{Q}(z) \begin{pmatrix} 0 & 1 \\ -A & 0 \end{pmatrix} \mathbf{Q}^{-1}(z) = \begin{pmatrix} iB_+ & 0 \\ 0 & iB_- \end{pmatrix}. \tag{4}$$

The operators $B_\pm$ are pseudo-differential operators (locally but not globally), and are often referred to as the single-square-root operators; for 'true-amplitude' applications, their subprincipal symbols have to be taken into account. [For an introduction to the notion of wave front sets and the calculus of pseudo-differential operators, see Sjöstrand & Grigis (1994).] There are several different choices possible for the 'normalization' of $\mathbf{Q}(z)$. We choose the vertical power flux normalization because in this normalization the operators $B_\pm$ are self-adjoint, and the diagonal entries of the coupling operator, $\mathbf{Q}(z)\partial_z\mathbf{Q}(z)^{-1}$, are of lower order and can be neglected in leading-order 'true-amplitude' applications. In this normalization, the decomposition operators take the form

$$\mathbf{Q}(z) = \frac{1}{2} \begin{bmatrix} Q_+^*(z)^{-1} & -\mathcal{H}Q_+(z) \\ Q_-^*(z)^{-1} & \mathcal{H}Q_-(z) \end{bmatrix}, \tag{5}$$

where the $Q_\pm(z)$ are pseudo-differential operators, and $\mathcal{H}$ is the Hilbert transform in time. System (1) transforms, upon suppressing the down–up coupling, into a system of one-way wave equations,

$$\partial_z \begin{pmatrix} u_+ \\ u_- \end{pmatrix} = \begin{pmatrix} iB_+ & 0 \\ 0 & iB_- \end{pmatrix} \begin{pmatrix} u_+ \\ u_- \end{pmatrix} + \begin{pmatrix} f_+ \\ f_- \end{pmatrix}, \tag{6}$$

for the downgoing field, u_+, and the upgoing field, u_-. From (3) we find that $u(z, .) = Q_+^*(z)u_+(z, .) + Q_-^*(z)u_-(z, .)$, while $f_\pm(z, .) = \pm\frac{1}{2}\mathcal{H}Q_\pm(z)f(z, .)$. We introduce the Green's functions, $G_\pm$, for the one-way wave equations; we denote the corresponding solution operators, that is, one-way propagators, by the same symbols. Here, the evolution coordinate is z. We then form the matrix

$$\mathbf{G} = \begin{pmatrix} G_+ & 0 \\ 0 & G_- \end{pmatrix}, \tag{7}$$

which is the down–up solution operator for the diagonal system (6).

To develop the scattering equations and formulate the inverse scattering problem, we decompose the velocity model into a background model $c_0(z, x)$, which is smooth and assumed to be known, and a contrast, $\delta c(z, x)$, which is to be determined. The contrast defines the perturbation,

$$\delta A = 2c_0^{-3}\delta c\,\partial_t^2 \tag{8}$$

of A in (2). With c_0 playing the role of c in the directional decomposition above, this naturally leads to the introduction of

$$V(z) = \mathbf{Q}(z) \begin{bmatrix} 0 & 0 \\ -\delta A(z, .) & 0 \end{bmatrix} \mathbf{Q}(z)^{-1}, \tag{9}$$

cf. (4). We then introduce $\widehat{V}$ according to $V = \widehat{V} \partial_t^2$. While neglecting the down–up coupling in the background model, the directional decomposition facilitates the identification of different orders of multiply scattered waves. The total scattered field is written in the form

$$\begin{pmatrix} \delta u \\ \partial_z \delta u \end{pmatrix} = \mathbf{Q}(z)^{-1} \begin{pmatrix} \delta u_+ \\ \delta u_- \end{pmatrix}, \quad \delta U = \begin{pmatrix} \delta u_+ \\ \delta u_- \end{pmatrix}, \tag{10}$$

cf. (3). The equation for δU then reads (Malcolm & de Hoop 2005, eq. 41),

$$\left(I - \partial_t^2 \mathbf{G} \widehat{V}\right) \delta U = \partial_t^2 \mathbf{G}(\widehat{V} U), \tag{11}$$

which has the form of a Lippmann–Schwinger equation (Lippmann & Schwinger 1950; Lippmann 1950), or equivalently

$$\left(I - \partial_t^2 \mathbf{G} \widehat{V}\right) (U_0 + \delta U) = U. \tag{12}$$

2.2 Recursions: forward and inverse scattering

Starting from (11) we can now set up a recursion to generate multiply scattered waves:

$$\delta U_1 = \partial_t^2 \mathbf{G}(\widehat{V} U), \quad \delta U_m = \partial_t^2 \mathbf{G}(\widehat{V} \delta U_{m-1}), m = 2, \ldots, M \tag{13}$$

so that $\sum_{m=1}^{M} \delta U_m$ generates δU. [As compared with the generalized Bremmer coupling series, $\mathbf{G}(\widehat{V} \partial_t^2 \cdot)$ can be identified with K · in de Hoop (1996); the second-order time derivative, however, requires additional care in the analysis.] Clearly, m counts the order of scattering; here, we consider $M = 3$. In a surface seismic experiment, ignoring free-surface effects, we can set the upgoing source $f_- = 0$ (at $z = 0$), while one observes the upcoming wave constituent, $Q_-^*(0) \delta u_-(0, ., ., .)$; we model data, d, upon subjecting this constituent to a further restriction to the acquisition geometry.

To develop a framework for inverse scattering, we rewrite (12) according to Malcolm de Hoop (2005, eqs 49 and 50) as

$$\partial_t^2 \mathbf{G} \widehat{V} (U + \delta U) = \delta U.$$

The reconstruction of the contrast is initiated by expanding $\widehat{V}$ into the sum $\widehat{V} = \sum_{m=1}^{M} \widehat{V}_m$. In the actual process, the equation above, and the recursion below, need to be subjected to a restriction to $z = 0$ after applying $Q_-^*(z)$. The reconstruction is usually driven by the single scattering operator derived from δU_1 in (13) using all the data; that is,

$$\delta U = \partial_t^2 \mathbf{G}(\widehat{V}_1 U), \tag{14}$$

$$-\partial_t^4 \mathbf{G}(\widehat{V}_1 \mathbf{G}(\widehat{V}_1 U)) = \partial_t^2 \mathbf{G}(\widehat{V}_2 U), \tag{15}$$

$$-\partial_t^6 \mathbf{G}(\widehat{V}_1 \mathbf{G}(\widehat{V}_1 \mathbf{G}(\widehat{V}_1 U))) - \partial_t^4 \mathbf{G}(\widehat{V}_1 \mathbf{G}(\widehat{V}_2 U)) - \partial_t^4 \mathbf{G}(\widehat{V}_2 \mathbf{G}(\widehat{V}_1 U)) = \partial_t^2 \mathbf{G}(\widehat{V}_3 U), \cdots \tag{16}$$

Here, we assume full illumination through the single scattering operator appearing on the right-hand sides of eqs (14)–(16). In other words we have thus far assumed that $\widehat{V}_1$ is determined everywhere from eq. (14) in which case multiply scattered artefacts are estimated from (15) and (16). If the data acquisition only results in partial illumination, however, we can complement this illumination by higher-order terms appearing on the left-hand sides of (15) and (16). For example, the illumination of $\widehat{V}_2$ is the same as of $\widehat{V}_1$ allowing the detection of artefacts; locally, where $\widehat{V}_1$ has not been illuminated through (14), one can fill in 'holes' by moving the corresponding contribution from the left-hand side in eq. (15) to the right-hand side of eq. (14). Indeed, the left-most terms in (15) and (16) can generate contributions that are effectively of first (or second) order, the other two terms on the left-hand side of (16) can generate contributions that are effectively of second order, etc. This approach is discussed in detail in the following subsection.

2.3 Illumination decomposition

In many configurations, there are regions where $\widehat{V}$ cannot be reached by singly scattered waves. Multiply scattered waves may serve as a remedy for these illumination gaps. To analyse this possibility, we introduce the illumination decomposition,

$$\widehat{V}_1 = \widehat{V}_1' + \widehat{V}_1'' + \widehat{V}_1''' + \ldots, \tag{17}$$

where $\widehat{V}_1'$ is the part of the model that has been illuminated by the recorded singly scattered data, $\widehat{V}_1''$ is the part of the model that is first illuminated by the doubly scattered data, $\widehat{V}_1'''$ is the part of the model first illuminated by triply scattered data, and so on. In the further analysis, we assume that the wave front sets (see Sjöstrand & Grigis 1994, for definitions) of $\widehat{V}_1', \widehat{V}_1'', \widehat{V}_1''', \ldots$ have no points in common. We proceed with a construction to image regions where singly scattered waves do not illuminate the structure of interest; such a construction was carried out for surface-related multiples in Berkhout & Verschuur (2006).

Substituting (17) into the expansion for $\widehat{V}$ yields

$$\widehat{V} = \widehat{V}_1' + \widehat{V}_1'' + \widehat{V}_1''' + \ldots + \sum_{m=2}^{M} \widehat{V}_m. \tag{18}$$
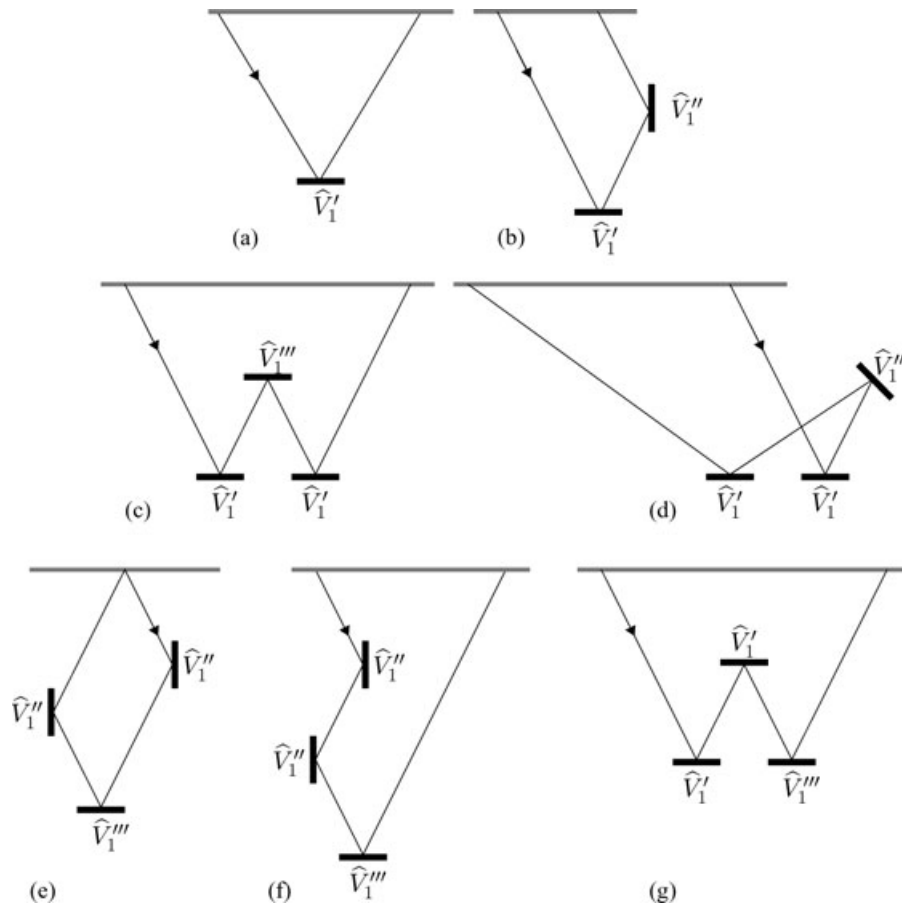
Figure 2. Illustration of some of the terms from eq. (19); (a) is singly scattered waves, (b) doubly scattered (from the second set of brackets), (c)–(g) are triply scattered contributions from the third bracketed term. In our formulation (c) and (d) are admitted while (e), (f) and (g) are not.

We note that the illumination decomposition pertains to the higher order terms, $\widehat{V}_2, \widehat{V}_3, \ldots$, associated with the artefacts, as well. Indeed, the artefact prediction is complicated by this decomposition.

We adapt the recursion in (14)–(16), by accounting for illuminating the contrast with multiply scattered waves. With the aid of (18), eq. (14) becomes

$$
\begin{aligned}
\delta U =\ & \partial_t^2 \mathbf{G}(\widehat{V}_1' U) + \partial_t^4 (\mathbf{G}(\widehat{V}_1' \mathbf{G}(\widehat{V}_1'' U)) + \mathbf{G}(\widehat{V}_1'' \mathbf{G}(\widehat{V}_1' U))) \\
& + \partial_t^6 (\mathbf{G}(\widehat{V}_1' \mathbf{G}(\widehat{V}_1''' \mathbf{G}(\widehat{V}_1' U))) + \mathbf{G}(\widehat{V}_1' \mathbf{G}(\widehat{V}_1' \mathbf{G}(\widehat{V}_1''' U))) + \mathbf{G}(\widehat{V}_1''' \mathbf{G}(\widehat{V}_1' \mathbf{G}(\widehat{V}_1' U))) \\
& + \mathbf{G}(\widehat{V}_1'' \mathbf{G}(\widehat{V}_1''' \mathbf{G}(\widehat{V}_1' U))) + \mathbf{G}(\widehat{V}_1' \mathbf{G}(\widehat{V}_1'' \mathbf{G}(\widehat{V}_1''' U))) + \mathbf{G}(\widehat{V}_1'' \mathbf{G}(\widehat{V}_1' \mathbf{G}(\widehat{V}_1'' U))) \\
& + \mathbf{G}(\widehat{V}_1' \mathbf{G}(\widehat{V}_1'' \mathbf{G}(\widehat{V}_1'' U))) + \mathbf{G}(\widehat{V}_1'' \mathbf{G}(\widehat{V}_1' \mathbf{G}(\widehat{V}_1'' U))) + \mathbf{G}(\widehat{V}_1''' \mathbf{G}(\widehat{V}_1'' \mathbf{G}(\widehat{V}_1' U))) \\
& + \mathbf{G}(\widehat{V}_1'' \mathbf{G}(\widehat{V}_1''' \mathbf{G}(\widehat{V}_1'' U))) + \mathbf{G}(\widehat{V}_1' \mathbf{G}(\widehat{V}_1'' \mathbf{G}(\widehat{V}_1''' U))) + \mathbf{G}(\widehat{V}_1''' \mathbf{G}(\widehat{V}_1'' \mathbf{G}(\widehat{V}_1'' U))) + \cdots
\end{aligned}
$$
(19)

which is then subjected to the restriction to the acquisition geometry in the plane $z = 0$. We note that eq. (19) closely resembles a Born scattering series. The key difference, however, is that we have replaced what would ordinarily be a single contrast V with three disjoint contrasts $\widehat{V}_1', \widehat{V}_1''$ and $\widehat{V}_1'''$ defining the different illumination characteristics of multiply scattered waves. Naturally, eqs (15) and (16) are affected by this refinement, and more intricate artefact contributions occur. This equation is illustrated in Fig. 2 which shows the first-order term [primary in (a)], the first of the two second-order terms [prismatic reflections in (b)], the two dominant third-order terms [multiples in (c) and (d)]. The bottom row of this figure shows three third-order scattering terms which are included in eq. (19) but will not be included in our algorithmic construction in the following section.

2.3.1 Down–up reduction

We simplify (19) following a seismic experiment. Considering typical scattering ray geometries in combination with a realistic acquisition geometry, we omit contributions that arise in the reconstruction of $\widehat{V}_1'''$ using $\widehat{V}_1''$ (see Figs 2e and f)—these are less likely to appear in the data. Contributions described by Fig. 2(g) are likely to violate our assumptions concerning the wave front sets of $\widehat{V}_1'$ and $\widehat{V}_1'''$. Out of the remaining

contributions involving $\widehat{V}_1'''$, the first term is most likely to play a role in practice (see Figs 2c and d). We define the components of $\widehat{V}$ as

$$\widehat{V} = \begin{pmatrix} \widehat{V}_{++} & \widehat{V}_{+-} \\ \widehat{V}_{-+} & \widehat{V}_{--} \end{pmatrix}. \tag{20}$$

We then assume that the effect of the free surface has been removed, the source is a downgoing wave

$$U = \begin{pmatrix} G_+ f_+ \\ 0 \end{pmatrix} \tag{21}$$

and that we record only the upgoing wavefield δu_- at the surface $z = 0$. With these assumptions, applying $Q_-^*(0)$, we obtain the data equation

$$\begin{aligned} d = \mathbf{R}\, Q_-^* \partial_t^2 G_- \big[(\widehat{V}_1')_{-+} &+ \partial_t^2 (\widehat{V}_1')_{-+} G_+ (\widehat{V}_1'')_{++} + \partial_t^2 (\widehat{V}_1'')_{--} G_- (\widehat{V}_1')_{-+} \\ &+ \partial_t^4 (\widehat{V}_1')_{-+} G_+ (\widehat{V}_1''')_{+-}\, G_- (\widehat{V}_1')_{-+} \big]\, G_+ f_+, \end{aligned} \tag{22}$$

where $\mathbf{R}$ stands for the restriction to $z = 0$ and d represents the reflection data. We have suppressed the further restriction to the acquisition geometry in our notation, however, we assume in the sequel that the acquisition geometry consists of a set of sources, s, each with an associated set, Σ_s, of receivers. The terms in this equation can be identified in Fig. 3. We will make use of eq. (22) in imaging by a bootstrapping argument. We note that the second and third terms on the right-hand side account for 'prismatic' reflections and that these two terms are reciprocal. The focus of this paper is the extension of standard imaging techniques that address the first term on the right-hand side to
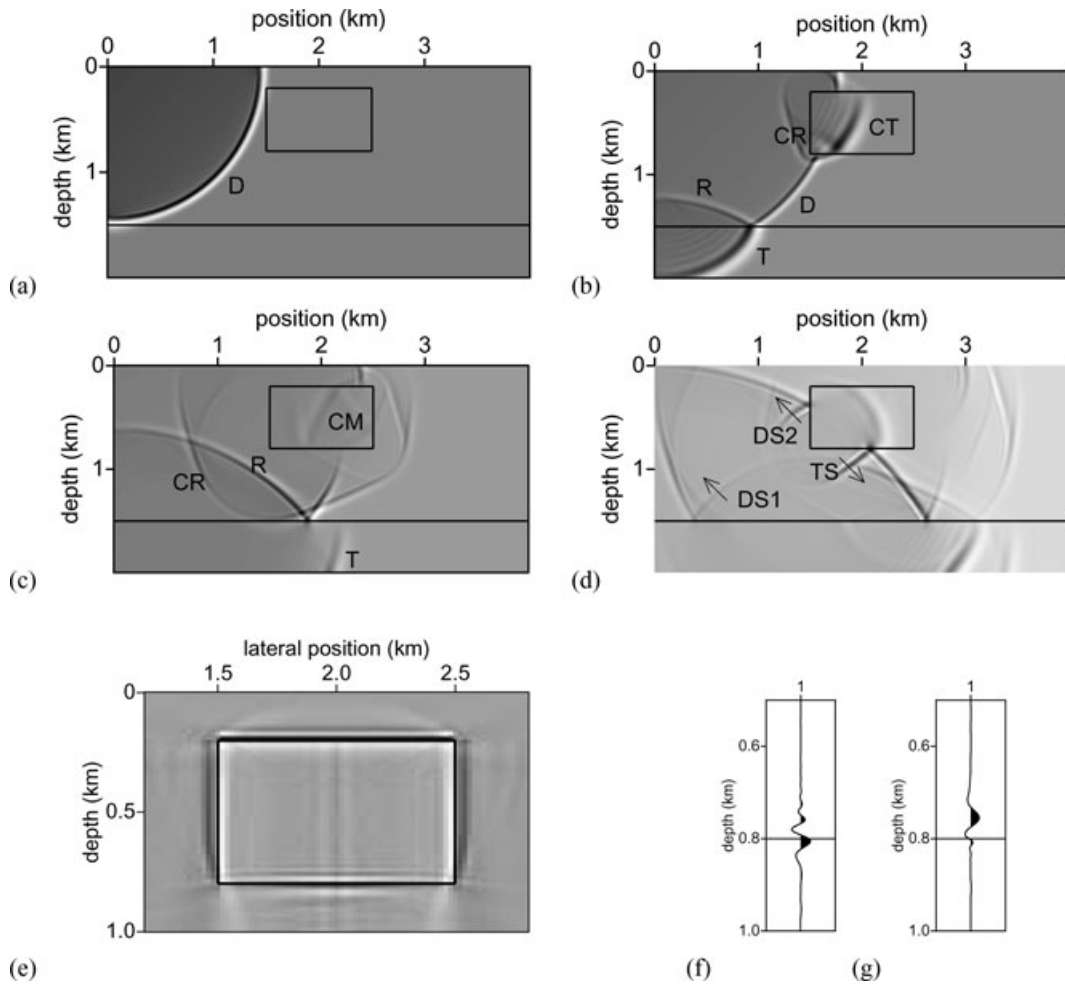

Figure 3. Using multiply scattered energy allows the full illumination of an object of interest from surface data. Here we illustrate both the data that are used in the imaging and the resultant images. In (a) through (d) we show snapshots of the wavefield, with time increasing from (a) to (d), as the data are generated. The annotations on the plots highlight different phases used in imaging; 'D' is the direct (downgoing) wave, 'R' is reflected (upcoming) from the lower reflector and 'T' is transmitted through it, 'CR' is the constituent reflected from the cube, 'CT' is the constituent transmitted into it, and 'CM' is the constituent multiply reflected within the cube; 'DS1' and 'DS2' are the doubly scattered waves off the left-hand vertical edge of the cube and 'TS' is the underside reflection. In all plots the solid lines mark the positions of reflectors. In (e) we show an image, made assuming constant background velocity, of the cube structure; the vertical edges are imaged with doubly scattered waves ['DS1' and 'DS2' in (d)] and the bottom with triply scattered waves ['TS' in (d)]. In (f) and (g) we show that imaging with triply scattered waves—and a constant background velocity—locates the reflector at the correct depth (in f), whilst imaging from above, shown in (g), naturally places the reflector at the wrong depth. The traces in (f) and (g) are stacks of images at the base of the cube; the solid line marks the correct reflector location.

include the fourth term, thus making use of 'underside' reflections. However, we will also briefly address the second and third terms in the discussion.

3 IMAGING WITH MULTIPLY SCATTERED WAVES

3.1 Projections

We begin from the data eq. (22). Our imaging strategy is as follows. We 'project' d onto d_1 in the range of the single scattering operator,

$$d_1 = \mathbf{R}\, Q_-^* \partial_t^2 G_-[(\widehat{V}_1')_{-+}(G_+ f_+)], \tag{23}$$

by minimizing $\|d - d_1\|$. In the process we reconstruct $(\widehat{V}_1')_{-+}$. This minimization differs from that used in Brown & Guitton (2005) to regularize their iterative inversion problem in that we directly project onto the data, whereas their regularization occurs in the image domain. In the context of our approach, we can introduce a penalizing term to the 'projection' that promotes contrast functions that differ from one another, consistent with the artefact identification procedure of Malcolm & de Hoop (2005). From the estimate of $(\widehat{V}_1')_{-+}$, we then select a part, $(\widehat{V}_1)_{-+}$, of the reconstruction of $(\widehat{V}_1')_{-+}$ to become a (or multiple) scatterer in the background model; these scatterers can be regularized and enhanced with the aid of a curvelet-like transform and methods of ℓ^1 optimization. In contrast to reverse-time methods (Mittet 2006) and the method of Youn & Zhou (2001) this scatterer is not picked and included in the velocity model but is derived from the data themselves. Using $(\widehat{V}_1)_{-+}$, we form a 'double' scattering operator by replacing G_- on the right-hand side of (23) by

$$\widetilde{G}_{-+}\cdot = \partial_t^2 G_-[(\widehat{V}_1)_{-+}(G_+ \cdot)]. \tag{24}$$

We proceed by 'projecting' $d - d_1$ onto d_2 in the range of the 'double' scattering operator,

$$d_2 = \mathbf{R}\, Q_-^* \partial_t^2 \widetilde{G}_{-+}[(\widehat{V}_1'')_{++}(G_+ f_+)], \tag{25}$$

by minimizing $\|(d - d_1) - d_2\|$. We reconstruct $(\widehat{V}_1'')_{++}$, and then repeat this step with the reciprocal form,

$$d_2 = \mathbf{R}\, Q_-^* \partial_t^2 G_-[(\widehat{V}_1'')_{--}(\widetilde{G}_{-+} f_+)], \tag{26}$$

and reconstruct $(\widehat{V}_1'')_{--}$. However, in the vertical acoustic power flux normalization, $\widehat{V}_{--} = \widehat{V}_{++}$, whence we take half the sum of the two double scattering reconstructions. Using $(\widehat{V}_1)_{-+}$, we form a 'triple' operator by replacing both G_- and G_+ on the right-hand side of (23) by $\widetilde{G}_{-+}$. We proceed with 'projecting' $d - d_1 - d_2$ onto d_3 in the range of the 'triple' scattering scattering operator,

$$d_3 = \mathbf{R}\, Q_-^* \partial_t^2 \widetilde{G}_{-+}[(\widehat{V}_1''')_{+-}(\widetilde{G}_{-+} f_+)], \tag{27}$$

by minimizing $\|(d - d_1 - d_2) - d_3\|$. From this, we obtain a reconstruction of $(\widehat{V}_1''')_{+-}$.

A natural concern is the separation of the ranges of the different scattering operators (i.e. isolating multiply scattered waves). Indeed, an estimate of $(\widehat{V}_1')_{-+}$ made by approximating d_1 with d will differ from the true $\widehat{V}$, by not only the illumination footprint of the acquisition geometry but also by artefacts from higher-order scattering (e.g. internal multiples). An approach to attenuate these artefacts is discussed in Malcolm & de Hoop (2005), which can be refined to account for the illumination decomposition introduced here. Moreover, the subtraction of data sets, $d - d_1$, $(d - d_1) - d_2$, and so on, with eqs (23)–(27) is problematic as the resolution of $d_1, d_2, \ldots$ will differ from one another.

The approach developed in this paper assumes that singly scattered waves illuminate structures only from above. Where strong vertical gradients exist, however, this assumption can be violated as waves will turn allowing the illumination of near-vertical reflectors (this is exploited in Shan & Biondi 2004; Xu & Jin 2006; Zhang *et al.* 2006) and, in extreme cases, even illuminating reflectors from below. In principle, we can accommodate these situations by introducing curvilinear coordinates.

3.2 Imaging condition

We revisit the imaging condition from a reverse-time migration perspective, allowing Green's functions in general background models. For each source, the incident field can be written in the form

$$u_s(z, \bar{x}, \omega) = G_+(z, \bar{x}, \omega, 0, s) \tag{28}$$

assuming that $f_+(x, \omega) = -\delta(x - s)$. To clarify the notation, $G_+(z, \bar{x}, \omega, 0, s)$ is the downgoing Green's function for a source excited at $(z = 0, x = s)$ at frequency ω and recorded at position $(z = z, x = \bar{x})$. The backpropagated data are given by

$$u_{\Sigma_s}(z, x, \omega) = \int_{\Sigma_s} \overline{G_-(0, r, \omega, z, x)}\, Q_{-,r}(0) d(r, \omega, s)\, \mathrm{d}r; \tag{29}$$

the subscript $_r$ in $Q_{-,r}$ signifies that the operator acts in the r, and not the s, variables. We note that the matrix elements of the operator $\widehat{V} = \widehat{V}(z) = \widehat{V}(z, x, D_x, D_t)$, such as

$$\widehat{V}_{-+}(z)\cdot = \mathcal{H}\, Q_-(z)\left(-c_0^{-3}\delta c(z, \cdot)(Q_+^*(z)\cdot)\right), \tag{30}$$

which contain the contrast $-c_0^{-3}\delta c$, can be written in terms of their kernels, $\widehat{V}(z, x, \bar{x}, \omega)$. We denote the image of $\widehat{V}_{-+}(z, x, \bar{x}, \omega)$ by $\mathcal{I}(z, \bar{x}, x, \omega)$. The imaging operator follows from the mapping $d(r, t, s) \mapsto I(z, \bar{x}, x)$, where $I(z, \bar{x}, x)$ is given by

$$I(z, \bar{x}, x) = \frac{1}{2\pi} \int \mathcal{I}(z, \bar{x}, x, \omega)\,\mathrm{d}\omega = \frac{1}{2\pi} \int\int \overline{u_s(z, \bar{x}, \omega)}u_{\Sigma_s}(z, x, \omega)\,\mathrm{d}s\omega^2\mathrm{d}\omega$$

$$\overset{\omega \to -\omega}{=} \frac{1}{2\pi} \int\int u_s(z, \bar{x}, \omega)\overline{u_{\Sigma_s}(z, x, \omega)}\,\mathrm{d}s\omega^2\mathrm{d}\omega, \tag{31}$$

where the second representation is obtained by time reversal. Using that $G_+(z, \bar{x}, \omega, 0, s)Q_{+,s}(0)$ can be identified with $Q_{-,s}^*(0)G_-(0, s, \omega, z, \bar{x})$, that is, reciprocity, the first representation attains the form used to image in the downward-continuation approach. With the modelling equation (*cf.* 23)

$$d(r, \omega, s) = Q_{-,r}(0)^*\omega^2 \int\int\int G_-(0, r, \omega, z, x)\widehat{V}_{-+}(z, x, \bar{x}, \omega)\, G_+(z, \bar{x}, \omega, 0, s)\,\mathrm{d}\bar{x}\mathrm{d}x\mathrm{d}z, \tag{32}$$

we can then form the normal equations and solve the inverse scattering problem by methods of least squares.

A standard calculation shows that an image of $-c_0^{-3}\delta c$ is obtained by setting, in (31), $\bar{x} = x$ after replacing $u_s(z, \bar{x}, \omega)$ by $Q_{+,\bar{x}}(z)^*u_s(z, \bar{x}, \omega)$ and replacing $u_{\Sigma_s}(z, x, \omega)$ by $-\mathcal{H}Q_{-,x}(z)^*u_{\Sigma_s}(z, x, \omega)$. We obtain a form resembling a two-way wave imaging procedure, but u_s does not propagate any $-$constituents while u_{Σ_s} does not propagate any $+$ constituents. If one were to use a two-way wave propagation procedure, one would filter out the respective constituents by methods of directional decomposition prior to applying the imaging condition to be consistent with the imaging procedure outlined above (Xie & Wu 2006).

One typically modifies the imaging operator derived from $I(z, x, x)$, in accordance with the *common-source* based normalization with the incoming wave amplitude (Claerbout 1971),

$$I(z, x) := \int I_s(z, x)\,\mathrm{d}s, \quad I_s^{(1)}(z, x) = \frac{1}{2\pi} \int \frac{1}{|u_s(z, x, \omega)|^2}\overline{u_s(z, x, \omega)}\, u_{\Sigma_s}(z, x, \omega)\,\mathrm{d}\omega. \tag{33}$$

This modification can be refined in accordance with a common-source (asymptotic) true-amplitude imaging condition:

$$I_s^{(2)}(z, x) = \frac{1}{2\pi} \int \frac{1}{|u_s(z, x, \omega)|^2}$$

$$\sum_{j=0}^n \overline{[A_j(z, x, \partial_x, \omega)u_s](z, x, \omega)}\, [A_j(z, x, \partial_x, \omega)u_{\Sigma_s}](z, x, \omega)\,(-\mathrm{i}\omega)^{-1}S(\omega)\mathrm{d}\omega, \tag{34}$$

where $A_0(z, x, \partial_x, \omega) = \mathrm{i}\omega c_0(z, x)^{-1}$, $A_1(z, x, \partial_z, \partial_x, \omega) = \partial_z$, and $A_{j+1}(z, x, \partial_z, \partial_x, \omega) = \partial_{x_j}$, $j = 1, \ldots, n-1$; $S(\omega) = \omega^{-2}$ if $n = 2$. This common-source imaging condition is obtained upon substituting asymptotic ray representations for the Green's functions. The operators A_j compensate, asymptotically, for the Jacobian following a transformation of coordinates such that Gel'fand's plane-wave expansion for the δ function can be applied. These operators also annihilate wave constituents that propagate from the source at $(0, s)$ towards (z, x). Fletcher *et al.* (2006) introduce an *ad hoc*, directionally damped non-reflecting wave equation for reverse-time migration. Essentially, our asymptotically true-amplitude imaging condition accomplishes the task of damping naturally.

Following the common-source least-squares formulation, leads to the modification

$$I_s^{(3)}(z, x) = \left[\int |u_s(z, x, \omega)|^2\omega^4\mathrm{d}\omega\right]^{-1} \frac{1}{2\pi} \int \overline{u_s(z, x, \omega)}u_{\Sigma_s}(z, x, \omega)\,\omega^2\mathrm{d}\omega; \tag{35}$$

essentially the gradient (image) is scaled with (an estimate of) the diagonal of the Hessian (Plessix & Mulder 2004); see also Shin *et al.* (2001). This approach can be extended to a least-squares formulation for 'all sources and receivers'. In this case, the division in eq. (35) may become unstable near zeros of u_s. Several options for regularizing this computation are given in Vivas *et al.* (2008); in particular, they suggest replacing $|u_s(z, x, w)|^2$ in the denominator with

$$\int |u_s(z, x, \omega)|^2\mathrm{d}x \tag{36}$$

in regions where $|u_s(z, x, \omega)|^2$ is below some threshold. In a slightly different context, Plessix & Mulder (2004) give four options for rapidly computing the diagonal of the Hessian in a stable way.

So far, we have considered the imaging and (least-squares) reconstruction of $(\widehat{V}_1')_{-+}$ according to (23). We can immediately generalize the procedure to the other reconstructions. For example, to reconstruct $(\widehat{V}_1''')_{+-}$, one replaces G_- and G_+ both by $\widetilde{G}_{-+}$. We note that the computation of the latter operator makes use of the prior reconstruction of $(\widehat{V}_1')_{-+}$.

3.3 Algorithm summary

The proposed algorithm can be summarized as follows:

(i) We downward/forward propagate the 'source' wavefield, u_s, and downward/backward propagate the 'receivers' wavefield, u_{Σ_s}.

(ii) We store both u_s and u_{Σ_s} at each depth.

(iii) We apply imaging condition (35) to obtain an estimate for $-c_0^{-3}\delta c$ from $\widehat{V}_1'$ throughout the model.

(iv) With the estimate of $-c_0^{-3}\delta c$ we form operators $\widehat{V}_{-+}$, *cf.* (30), and apply these to u_s and u_{Σ_s} at each depth.

(v) We, accumulatively, propagate the outcomes of the previous step upward to form $\widetilde{u}_s$ (forward) and $\widetilde{u}_{\Sigma_s}$ (backward); $\widetilde{u}_s$ is obtained from u_s upon replacing G_+ by $\widetilde{G}_{-+}$, and $\widetilde{u}_{\Sigma_s}$ is obtained from u_{Σ_s} upon replacing $\overline{G_-}$ by $\overline{\widetilde{G}_{-+}}$.

(vi) We apply the imaging condition, using $\widetilde{u}_{\Sigma_s}$ and u_s to estimate $-c_0^{-3}\delta c$ from $\widehat{V}_1''$ in accordance with (25), and using $\widetilde{u}_{\Sigma_s}$ and $\widetilde{u}_s$ to estimate $-c_0^{-3}\delta c$ from $\widehat{V}_1'''$ in accordance with (27).

All computations are carried out in the frequency domain. In the above, we have omitted the subtraction, $d - d_1$ for the imaging with doubly scattered waves, and $d - d_1 - d_2$ for the imaging with triply scattered waves. This is motivated by computational efficiency. The idea is to apply pseudo-differential cut-offs to the downward continued fields, chosen in accordance with the reliable part of the background velocity model, prior to applying the imaging condition, to mimic the subtraction. Defining the reliable part of the model and determining the most advantageous variables in which to apply the cut-off functions may become delicate in complicated geologic settings and improving this aspect of the approach is the subject of ongoing research.

One such cut-off is illustrated in Fig. 4 for the double scattering case. The representative model consists of a vertical reflecting segment, and a deep, extended horizontal reflector. In (b) the backpropagated field u_{Σ_s} is shown at a certain depth (300 m, here); clearly d_1 (reflection off the bottom reflector) and d_2 ('prismatic' reflection) components are present. By applying a left–right separating 'dip' filter [in (c)], the two components separate sufficiently to prevent constructive correlation with $\widetilde{u}_s$, which is illustrated in (e) and is subjected to left–right separating 'dip' filtering as well [in (f)]. For comparison, we show the outcome of the subtraction procedure proper in (i). We note that the images obtained with filtering [in (h)] and with subtraction [in (i)] are very close to one another. The effect of ignoring the subtraction altogether is illustrated in the image in (g).

The cut-off used to mimic the subtraction $d - d_1 - d_2$ in the case of a typical triple scattering situation is illustrated in Figs 5–6. The representative model consists of a shallow horizontal reflecting segment, and a deep, extended horizontal reflector. To replace the subtraction of d_1, a straightforward windowing procedure is applied as illustrated in Fig. 5. The windowing is carried out while the data are downward continued, by removing a window of time before times where energy from multiples is expected. We use a time window that increases linearly with offset to account for moveout. Figs 5(b)–(e) show the data (u_{Σ_s}) at the depth of the upper reflector (segment); it is here that applying the imaging condition should result in the imaging (from below) of this reflector. In Fig. 5(b) the data are shown without the windowing procedure (which is applied on the way down and not at this point), so that the primary from the lower reflector is still visible, resulting in an artefact in the associated image (in Fig. 6a). In Fig. 5(c) the results of applying the windowing procedure are shown; despite the simplicity of this procedure, we note that the artefacts are attenuated in image shown in Fig. 6(b). For comparison, in Fig. 6(c), we show the image obtained with the subtraction procedure. In Fig. 5(e) we illustrate $\widetilde{u}_s$ at the depth of the upper reflector—no windowing needs to be applied.

4 NUMERICAL EXPERIMENTS: IMAGING WITH UNDERSIDE REFLECTIONS

In this and the next section, we present several synthetic data examples to demonstrate the utility of the method discussed above. The data were generated using a 2-D finite difference code; they were then filtered with a trapezoidal filter with corner frequencies 10 and 50 Hz and 10 Hz roll-off. The sources and receivers are positioned on (different) fixed grids. Table 1 summarizes the parameters used for each of the subsequent models used in the numerical experiments.

A problem of current interest in subsalt imaging is the location of the bottom of salt when the salt itself is non-uniform. Multiples can illuminate these structures without passing through them, however, and so have the potential to locate the salt bottom without first determining an accurate salt model. To test such a scenario, we developed a salt model in which the salt contains sediment inclusions; we then study the influence of these inclusions on the location of the bottom of salt both with singly and triply scattered waves. We generated data in two models: the 'inclusion model' and the 'inclusion-free model'. The inclusion model is shown in Fig. 7(a); the inclusion-free model differs only in the absence of the inclusions. Figs 7(b) and (c) show, respectively, a typical shot record in the inclusion model and the difference between this shot record in the inclusion and inclusion-free models illustrating just how significant the inclusions are to the wavefield. Fig. 8 shows two images, made with data generated in the inclusion model, one using the inclusion model and the other using the inclusion-free model. If the inclusions are unknown, we observe that the image of the base of salt deteriorates significantly, as expected.

In Fig. 9 we confirm that the base of salt can be imaged with underside reflections essentially as successfully as with topside reflections with realistic acquisition geometries if a good estimate of the salt body is known. However, the main advantage of imaging with internal multiples is that they might reflect off the base and flanks of the salt without passing through it, allowing imaging without knowing the structure of the salt. To test this, we restrict the source–receiver locations to avoid waves that pass through the salt. This is illustrated in Figs 10(a)–(c); in Fig. 10(a) the left-hand flank of the salt is imaged using sources (whose range is denoted with the black line) and receivers (whose range is denoted with the white line and extends to 0 off the edge of the plot) to the left-hand side of the salt body. This restricts our wave paths to those illustrated in Fig. 2(d). In Fig. 10(b) the sources are to the left-hand side of the salt and the receivers to the right, focusing on paths like those illustrated in Fig. 2(c); we observe that the base of salt is well imaged. Fig. 10(c) shows a reconstruction of the lower half of the salt body formed by summing three images made using different source–receiver geometries.

In Fig. 11, we demonstrate the insensitivity of our procedure to errors in the velocity model. Figs 11(a)–(c) are analogous to Figs 10(a)–(c) with the exception that the data were modelled in the inclusion model. These data were still imaged using the inclusion-free model and yet the (partial) images remain of the same quality as those shown in Fig. 10 where there were no inclusions. The images in Figs 11(c) and 8(a) compare favourably. To further emphasize this point, in Fig. 12 we show an amplitude extraction along the base of the salt done for three
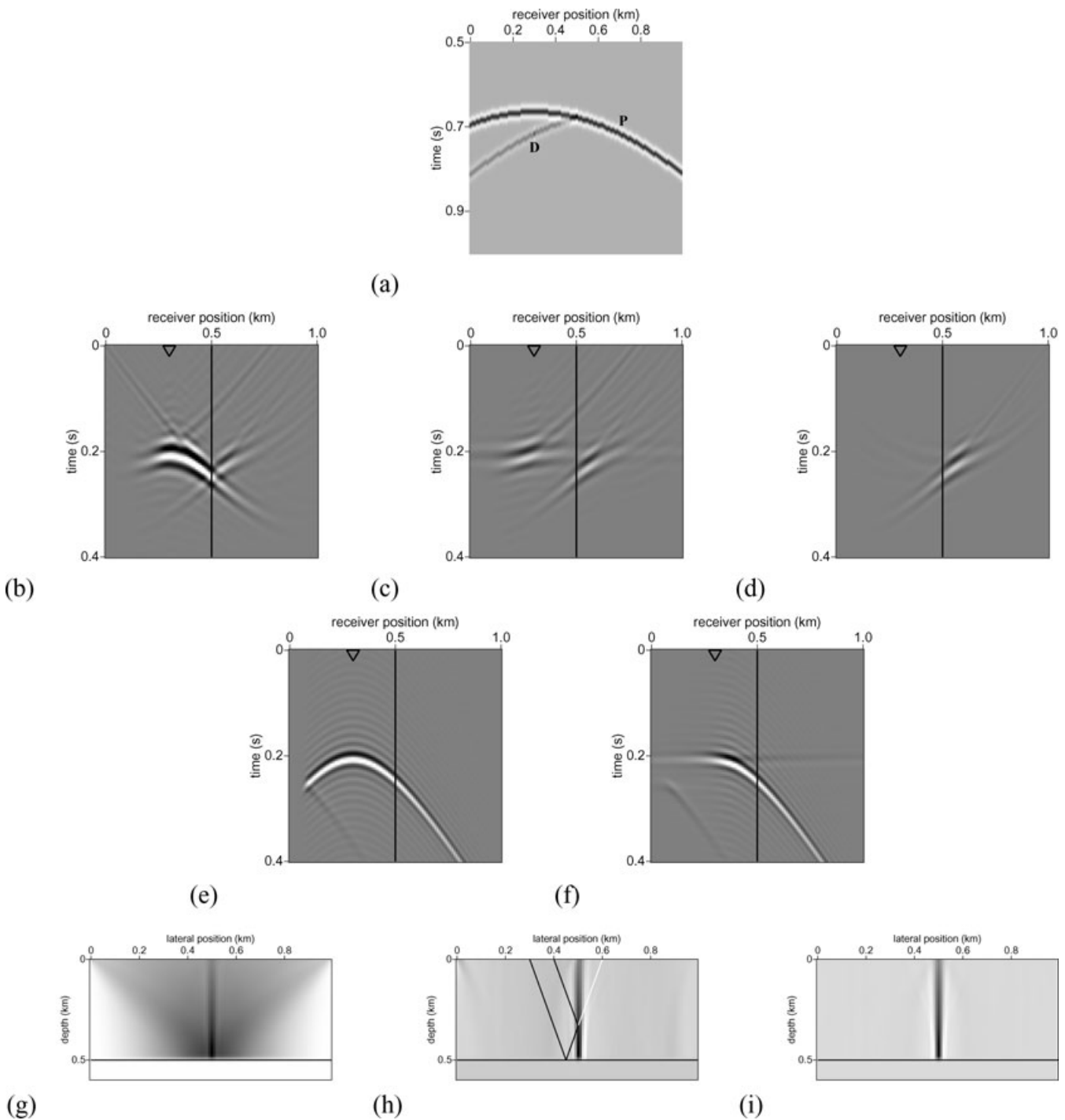
Figure 4. (a) Shot record, with source s at 0.3 km [indicated by a triangle in (b)–(d)]; 'P' marks the primary reflection off the bottom reflector and 'D' marks the doubly scattered wave; (b) the field u_{Σ_s} at a depth of 0.3 km (the vertical line indicates the fault location); (c) the field u_{Σ_s} at a depth of 0.3 km subjected to left–right 'dip' filtering, suppressing the white ray in (g); (d) the field u_{Σ_s} at a depth of 0.3 km generated from $d - d_1$; (e) the field $\tilde{u}_s$ at a depth of 0.3 km; (f) the field $\tilde{u}_s$ at a depth of 0.3 km subjected to left–right 'dip' filtering; (g) image generated omitting the subtraction procedure; (h) image generated with the filtering and (i) image generated with the subtraction procedure.

different images; the image in the inclusion model with the correct velocity model, the image made with the same data using the inclusion-free velocity model and the triply scattered image. Fig. 12(a) shows the locations of the points around which the amplitude is extracted and (b) shows the maximum amplitude within a wavelength of these points, smoothed with a 3 point median filter. The variations in the extracted amplitude for the image made in the correct velocity model are caused by the inclusions themselves; we have not included illumination corrections. The low regions in the multiply scattered image are where no data are available with neither the source nor receiver leg passing through the salt.
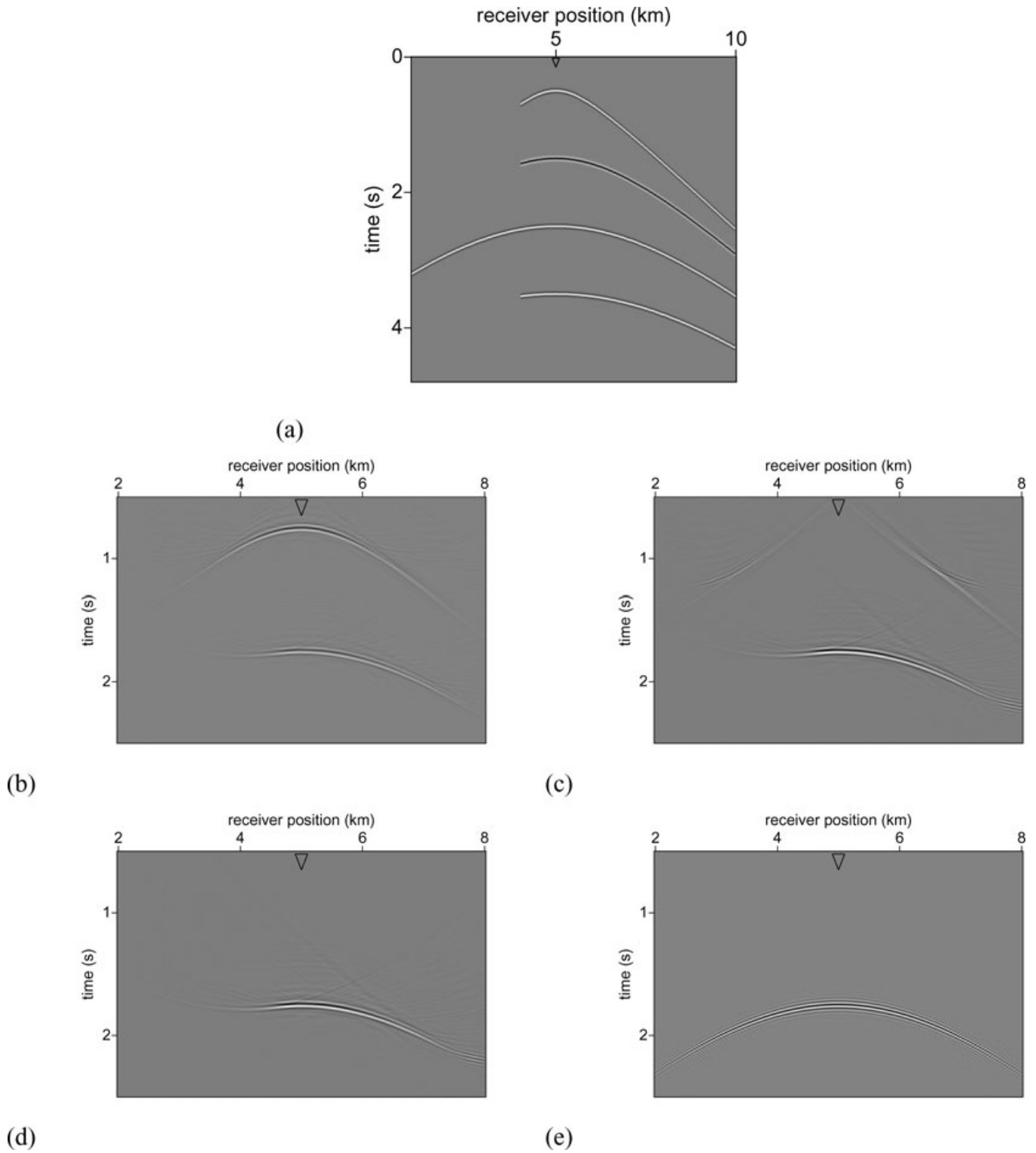
Figure 5. (a) Shot record, with source s at 5 km [indicated by a triangle in (b)–(e)]; (b) the field u_{Σ_s} at a depth of 1.5 km; (c) the field u_{Σ_s} at a depth of 1.5 km subjected to time-windowing, suppressing primary reflections; (d) the field u_{Σ_s} at a depth of 1.5 km generated from $d - d_1(-d_2)$; (e) the field $\tilde{u}_s$ at a depth of 1.5 km.

Table 1. Parameters used to generate the example synthetic data sets.

Model	First r (km)	Δr (m)	# Receivers	First s (km)	Δs (m)	# Sources
Salt	0	20	650	2.0	100	80
Fault	0	20	550	0	100	110
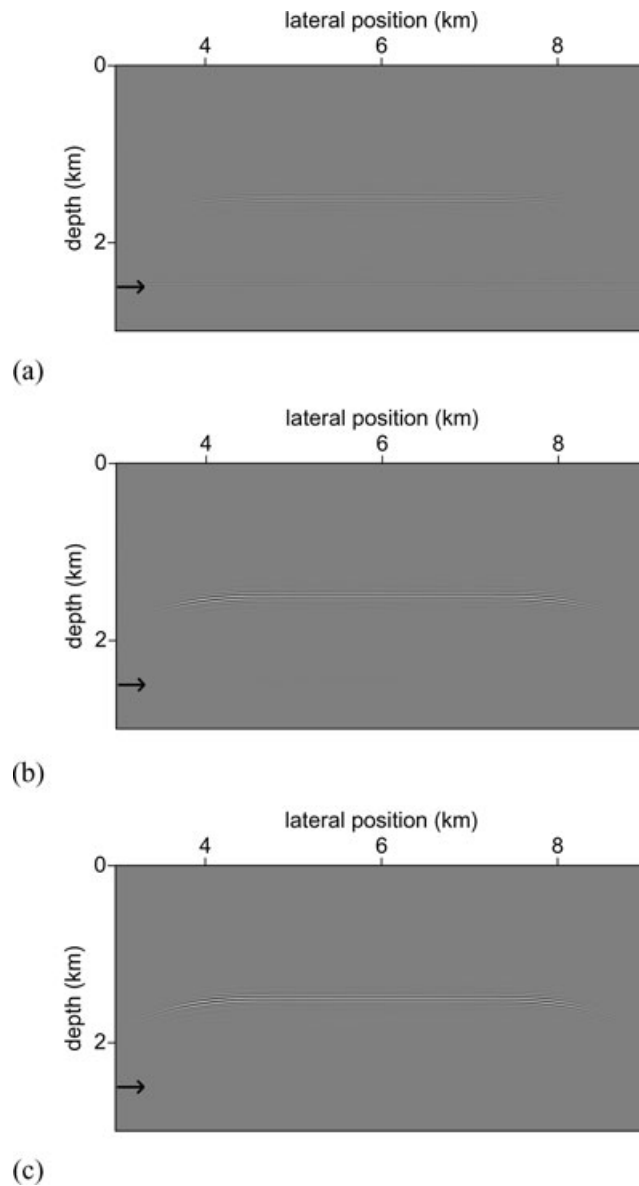
Figure 6. (a) Image generated omitting the subtraction procedure; (b) image generated with the windowing and (c) image generated with the subtraction procedure. The arrow indicates the depth of the bottom reflector.

5 DISCUSSION

By including the illumination footprint of the acquisition geometry from the beginning of our, series based, data representation we are able to split off contributions from different orders of scattering. From these separated contributions it is possible to develop an algorithm to treat each order of multiple scattering independently. Thus far, we have focused on the use of 'underside' reflections, but 'prismatic' reflection are included in our approach as well as illustrated in the next paragraph. It is important to note that the algorithms for doubly and triply scattered imaging are quite similar and can in fact be combined into one multiple-scattering imaging algorithm leading to illumination, in principle, from all sides.

5.1 Imaging with 'prismatic' reflections

Along with subsalt imaging from below, the approach presented above also allows the imaging of steeply dipping reflectors with doubly scattered waves in a manner similar to the one discussed by Jin *et al.* (2006) and Xu & Jin (2007). In a numerical experiment, here, we focus on imaging faults. The model, shown in Fig. 13(a), consists of sedimentary layers with simple topography cut through by a fault structure. A standard image based on primary reflections is shown in Fig. 13(b), in which the fault's location is perhaps discernible but it has not been imaged. This figure [in (c)] also shows the difference of two images made with doubly scattered waves, one with waves reflected off the
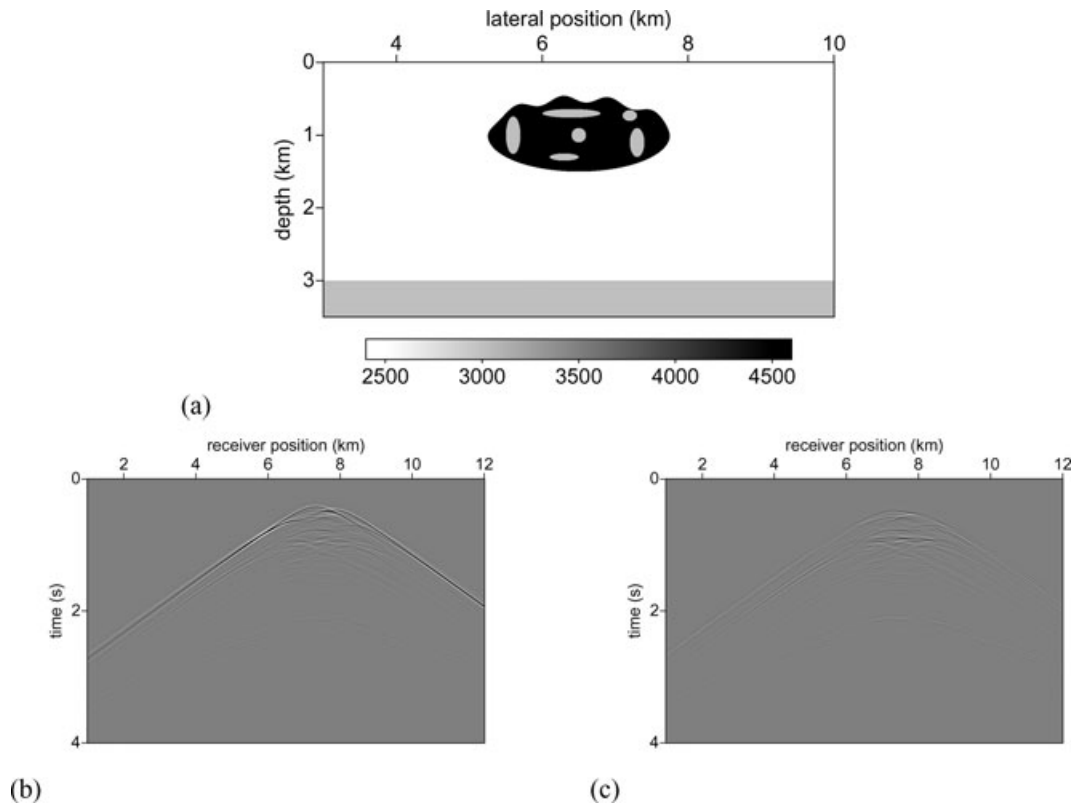
Figure 7. (a) Velocity model for the salt example, the normal incidence reflection coefficient for the top of salt is 0.29 and for the deep lower reflector is 0.09; (b) shot record at $s = 5.5$ km and (c) difference between shot records with and without inclusions.
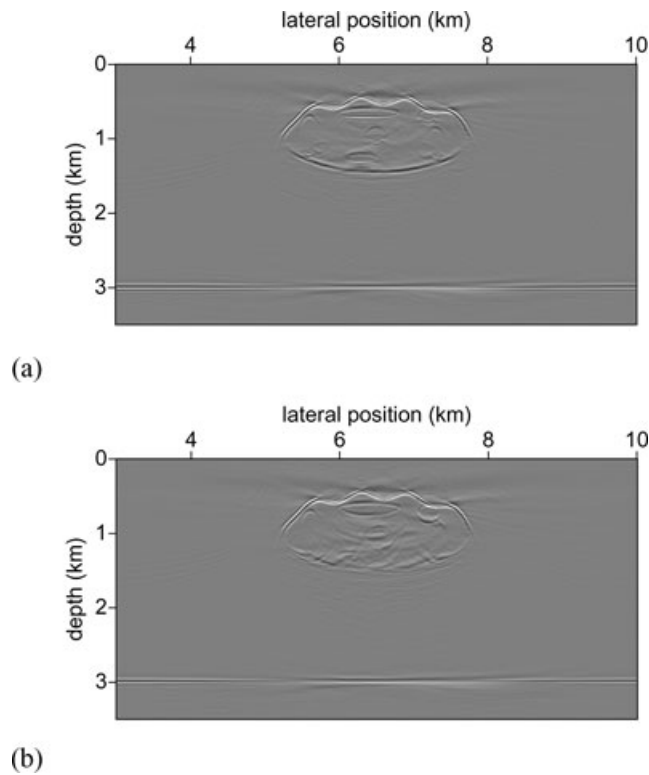

Figure 8. (a) Image based on primary reflections made with the correct velocity model using the model and data illustrated in Fig. 7—the best image we can expect to make of the bottom of the salt; (b) image based on primary reflections made with the inclusion-free velocity model.
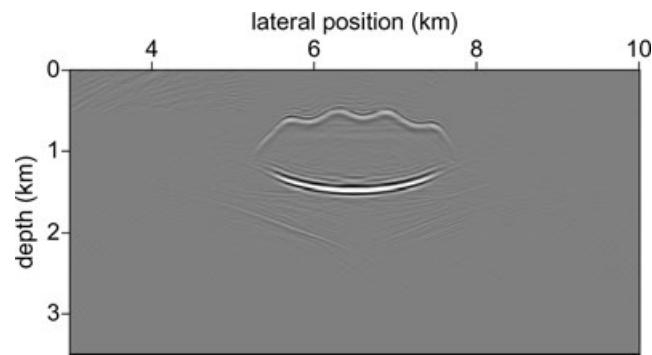
Figure 9. Imaging with underside reflections using offsets up to 6 km; the triply scattered waves propagate through the salt. This image illustrates that, under idealized circumstances, underside reflections and topside reflections can be used in a similar way in non-trivial structures.
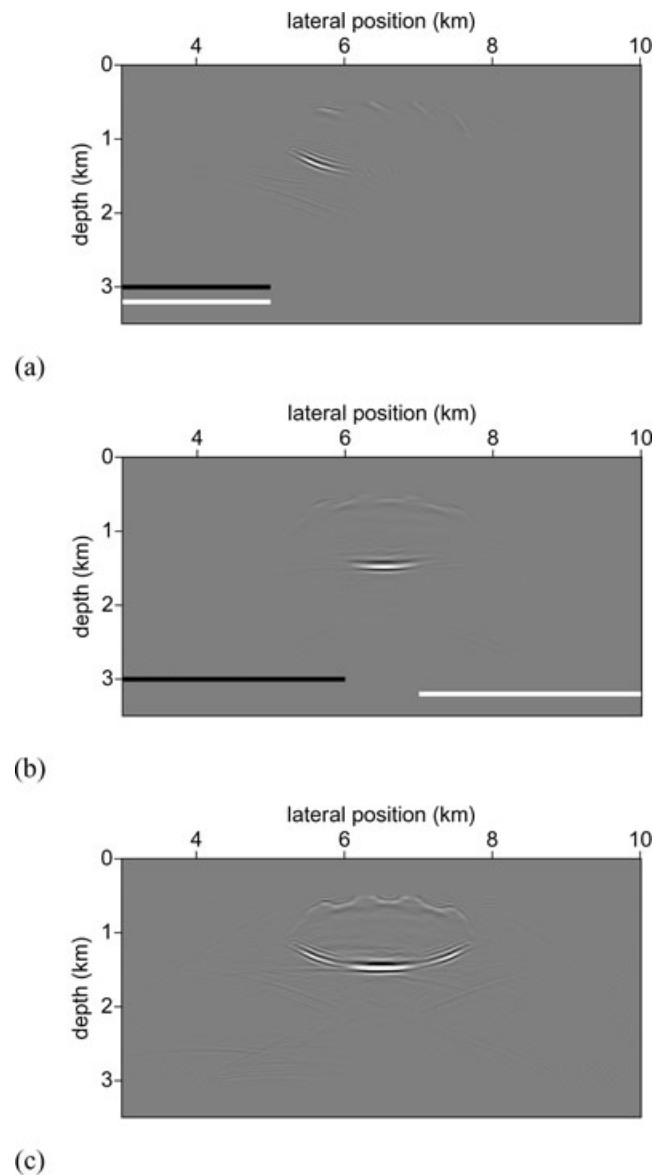
(a)

(b)

(c)

Figure 10. Imaging with underside reflections, using data generated in the model without inclusions; (a) left-hand lower flank of the salt imaged using sources (whose range is denoted with the black line) and receivers (whose range is denoted with the white line and extends to 0 off the edge of the plot) to the left-hand side of the salt body—wave paths corresponding with Fig. 2(d); (b) bottom of the salt imaged using sources to the left-hand side of the salt and receivers to the right, focusing on paths like those illustrated in Fig. 2(c); (c) reconstruction of the lower part of the salt body formed by adding (a), (b) and an image generated as in (a) but with sources and receivers to the right-hand side of the salt body.
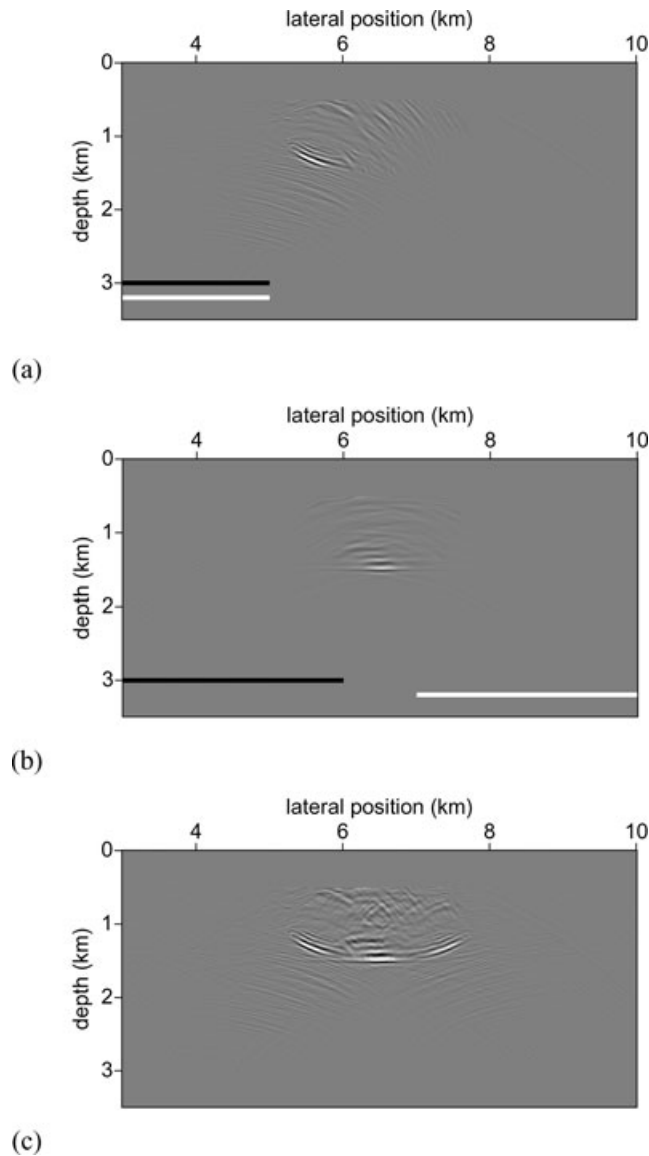
Figure 11. Imaging using the inclusion-free model as velocity model with underside reflections, using data generated in the model with inclusions; (a) left-hand lower flank of the salt imaged using sources (whose range is denoted with the black line) and receivers (whose range is denoted with the white line and extends to 0 off the edge of the plot) to the left-hand side of the salt body—wave paths corresponding with Fig. 2(d); (b) bottom of the salt imaged using sources to the left-hand side of the salt and receivers to the right, focusing on paths like those illustrated in Fig. 2(c); (c) reconstruction of the lower part of the salt body formed by adding (a), (b) and an image generated as in (a) but with sources and receiver to the right-hand side of the salt body.

left-hand side of the fault and the other with waves reflected off the right-hand side of the fault. This doubly scattered image is then added to the regular image resulting in an image where near-vertical and near-horizontal structures are well resolved [in (d)].

Note that contrary to the subsalt imaging example given in the previous section, in the fault imaging example $(\widehat{V}_1)_{-+}$ contains multiple reflectors. This emphasizes that the theory presented here does not require the identification of a single multiple-generating interface but instead works with all interfaces imaged by a standard migration. In fact, including multiple reflectors in $(\widehat{V}_1)_{-+}$ introduces redundancy in as much as different multiples of the same (third) order illuminate the same structure using different reflectors as the deep reflection point. This is in addition to the usual redundancy over sources and receivers that is, of course, necessary to form $(\widehat{V}_1)_{-+}$ or $(\widehat{V}_1''')_{+-}$.

5.2 Some practical issues

This study has dealt primarily with theoretical aspects of this approach; an application to field data is the subject of continuing research. To apply this method to field data, several practical issues must be adequately addressed. The first is the estimation of the windowing functions used to separate primaries and multiples and the filters used to separate doubly and singly scattered waves. Both of these may require a refinement for applications to real data; studying the issues associated with real data may also lead to more robust methods of performing this separation. Second, as in most methods which combine different data sets to form multiply scattered waves [here the data themselves and
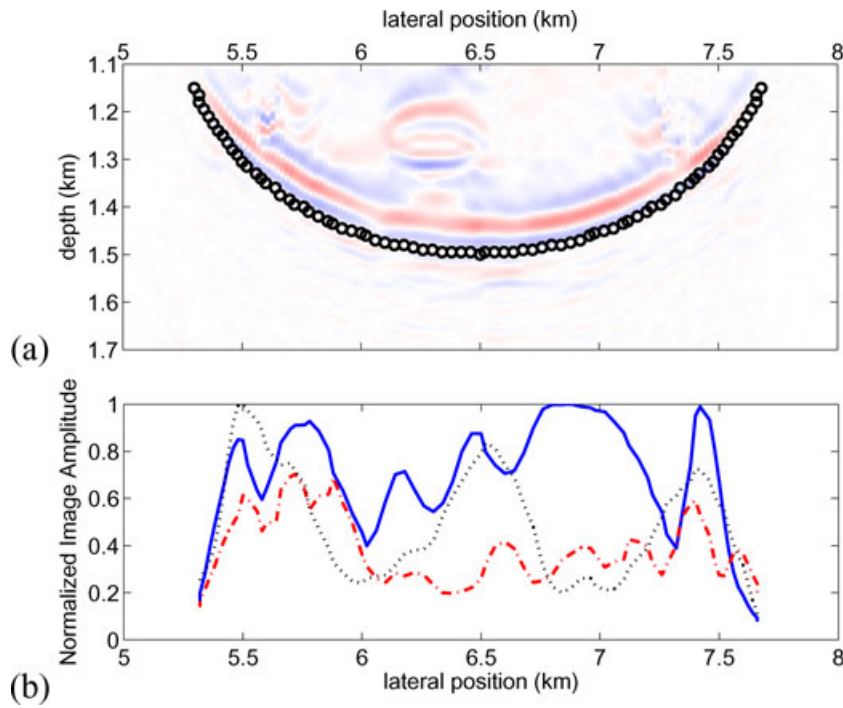
Figure 12. Amplitude extraction along the base of salt. The maximum amplitude within one wavelength of the set of points shown in (a) overlain on the image from Fig. 8(a) is plotted in (b) for each of three images. The 'perfect' image made with singly scattered data shown in Fig. 8(a) (solid blue line), the image, shown in Fig. 8(b) made with the inclusion-free velocity model (dashed red line) and the image shown in Fig. 10(c) made with multiply scattered waves from below the salt (dotted black line). Both primary images are normalized by the maximum amplitude in the image made with the correct velocity model; the triple scattered image is normalized to its maximum value. The lines have been smoothed with a 3-point median filter.
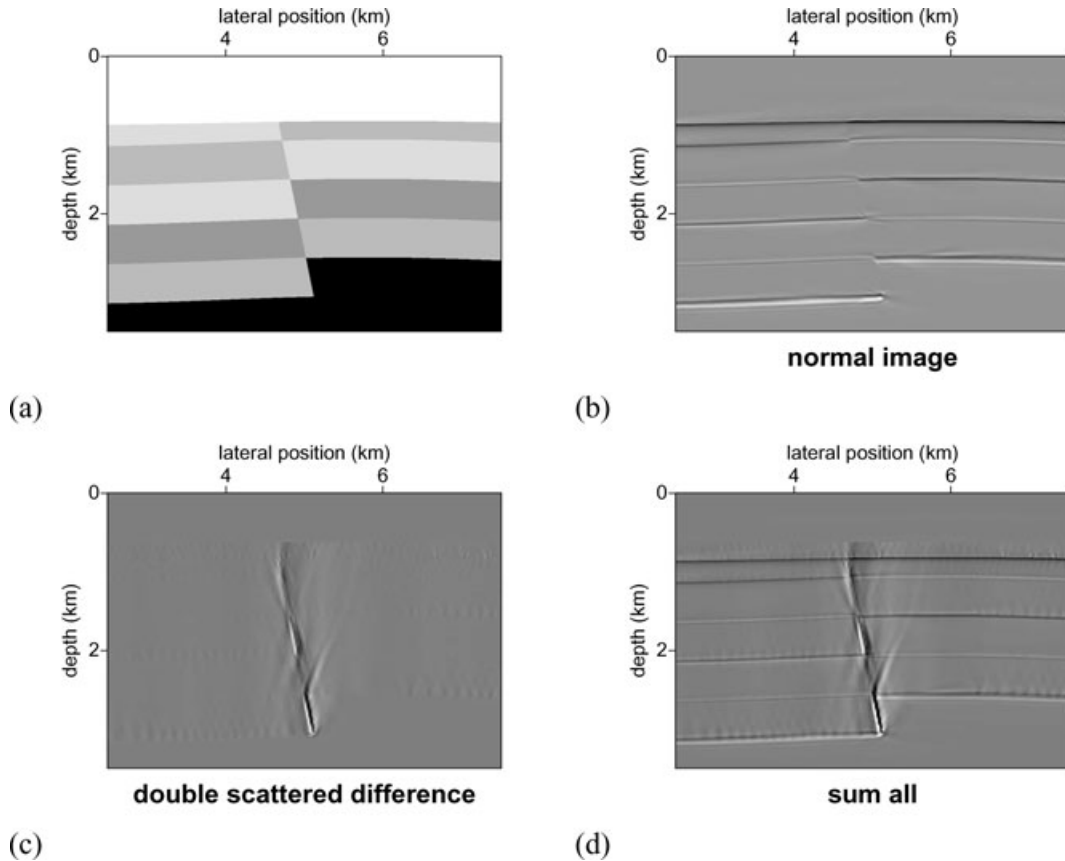

Figure 13. (a) Velocity model for the fault model; (b) standard image based on primary reflections; (c) image based on prismatic reflections (doubly scattered waves), taking the difference of the left- and right-hand side scattered contributions; (d) the sum of (b) and (c).

the image, $(\hat{V}_1)_{-+}$, formed from the data], we will require an estimate of the source signature. This can be seen, for example, in Fig. 9 in which the image of the base of salt has more zero crossings than does the image made with singly scattered waves. The importance (and ease) of this step will be data dependent. Third, though the theory presented here is equally applicable in three dimensions we have chosen to compute only 2-D examples. Although the extension of the algorithm to three dimensions is straightforward, practical issues such as computation time and storage of the intermediate data fields will become significantly more important in three dimensions. These problems can be mitigated by using efficient 3-D propagators and by storing the wavefield at depth in only a limited region.

6 CONCLUSIONS

Multiply scattered waves, specifically internal multiples, have the ability to contribute reliable information to seismic images. Because they can illuminate structures not easily illuminated by primaries, these waves allow us to image portions of the subsurface not illuminated by singly scattered energy. We have presented a computational and processing-based approach to image with multiply scattered waves. The fundamental assumption necessary to our method is that the multiply scattered waves reflect from at least one smooth reflector beneath the structure of interest before illuminating this structure; we also require that this reflector be at least partly imaged by singly scattered waves. This translates into a requirement of wide-angle data so that both the necessary (internal) multiply scattered waves, and primaries with which to image the lower reflector are recorded. We anticipate the key applications of this method to occur in subsalt imaging but, as our method depends on estimates of part of the migration velocity model (though not within salt, for example), incorporation of multiply scattered waves in migration velocity analysis seems feasible along the same line of reasoning as presented by Verschuur & Berkhout (2007) for surface-related multiples. Through synthetic data examples, we have demonstrated the ability of our method to use various types of internal multiples to image structures that cannot normally be imaged from surface data.

ACKNOWLEDGMENTS

REFERENCES

Bell, D.W., 1991. Seismic imaging of steeply dipping geologic interfaces, United States patent, 4987561.

Berkhout, A.J. & Verschuur, D.J., 2006. Imaging of multiple reflections, *Geophysics,* **71**(4), SI209–SI220.

Berkhout, A.J. & Vershuur, D.J., 1994. Multiple technology. Part 2: migration of multiple reflections, *SEG Tech. Prog. Expand. Abstr.,* **13**(1), 1497–1500.

Biondi, B. & Shan, G., 2002. Prestack imaging of overturned reflections by reverse time migration, *SEG Tech. Prog. Expand. Abstr.,* **21**(1), 1284–1287.

Bostock, M.G., Rondenay, S. & Shragge, J., 2001. Multiparameter two-dimensional inversion of scattered teleseismic body waves 1. Theory for oblique incidence, *J. geophys. Res.,* **106**, 30 771–30 782.

Bremmer, H., 1951. The W. K. B. Approximation as the first term of a geometric-optical series, *Commun. Pure Appl. Math.,* **4**, 105–115.

Broto, K. & Lailly, P., 2001. Towards the tomographic inversion of prismatic reflections, *SEG Tech. Prog. Expand. Abstr.,* **20**(1), 726–729.

Brown, M.P. & Guitton, A., 2005. Least-squares joint imaging of multiples and primaries, *Geophysics,* **70**(5), S79–S89.

Cavalca, M. & Lailly, P., 2005. Prismatic reflections for the delineation of salt bodies, *SEG Tech. Prog. Expand. Abstr.,* **24**(1), 2550–2553.

Cavalca, M. & Lailly, P., 2007. Accounting for the definition domain of the forward map in traveltime tomography – application to the inversion of prismatic reflections, *Inverse Problems,* **23**, 139–164.

Cheney, M. & Bonneau, R.J., 2004. Imaging that exploits multipath scattering from point scatterers, *Inverse Problems,* **20**(5), 1691–1711.

Claerbout, J.F., 1971. Toward a unified theory of reflector mapping, *Geophysics,* **36**(3), 467–481.

de Hoop, M.V., 1996. Generalization of the Bremmer coupling series, *J. Math. Phys.,* **37**, 3246–3282.

de Hoop, M.V. & Uhlmann, G., 2006. Characterization and 'source-receiver' continuation of reflection seismic data, *Comm. Math. Phys.,* **263**, 1–19.

Fletcher, R.P., Fowler, P.J., Kitchenside, P. & Albertin, U., 2006. Suppressing unwanted internal reflections in prestack reverse-time migration, *Geophysics,* **71**(6), E79–E82.

Guitton, A., 2002. Shot-profile migration of multiple reflections, *SEG Tech. Prog. Expand. Abstr.,* **21**(1), 1296–1299.

Hale, D., Hill, N.R. & Stefani, J.P., 1991. Imaging salt with turning seismic waves, *SEG Tech. Prog. Expand. Abstr.,* **10**(1), 1171–1174.

Hawkins, K., 1994. The challenge presented by North Sea Central Graben salt domes to all DMO algorithms, *First Break,* **12**, 327–343.

Jiang, Z., 2006. Migration of interbed multiple reflections, *SEG Tech. Prog. Expand. Abstr.s,* **25**(1), 3501–3505.

Jiang, Z., Sheng, J., Yu, J., Schuster, G.T. & Hornby, B.E., 2007. Migration methods for imaging different-order multiples, *Geophys. Prospect.,* **55**(1), 1–19.

Jin, S., Xu, S. & Walraven, D., 2006. One-return wave equation migration: imaging of duplex waves, *SEG Tech. Prog. Expand. Abstr.,* **25**(1), 2338–2342.

Lippmann, B.A., 1950. Variational principles for scattering processes. II Scattering of slow neutrons by para-hydrogen, *Phys. Rev.,* **79**(3), 481–486.

Lippmann, B.A. & Schwinger, J., 1950. Variational principles for scattering processes I, *Phys. Rev.,* **79**(3), 469–480.

Malcolm, A.E. & de Hoop, M.V., 2005. A method for inverse scattering based on the generalized Bremmer coupling series, *Inverse Problems,* **21**, 1137–1167.

Malcolm, A.E., de Hoop, M.V. & Calandra, H., 2007. Identification of image artifacts from internal multiples, *Geophysics,* **72**(2), S123–S132.

Marmalyevskyy, N., Roganov, Y., Gornyak, Z., Kostyukevych, A. & Mershchiy, V., 2005. Migration of duplex waves, *SEG Tech. Prog. Expand. Abstr.,* **24**(1), 2025–2028.

Mittet, R., 2006. The behaviour of multiples in reverse time migration, in *Expanded Abstracts,* Eur. Assn. Geoscient. Eng.

Muijs, R., Robertsson, J.O.A. & Holliger, K., 2007a. Prestack depth migration of primary and surface-related multiple reflections. Part I—imaging, *Geophysics,* **72**(2), S59–S69.

Muijs, R., Robertsson, J.O.A. & Holliger, K., 2007b. Prestack depth migration of primary and surface-related multiple reflections. Part II—Identification and removal of residual multiples, *Geophysics,* **72**(2), S71–S76.

Nolan, C.J., Cheney, M., Dowling, T. & Gaburro, R., 2006. Enhanced angular resolution from multiply scattered waves, *Inverse Problems,* **22**, 1817–1834.

Plessix, R.-E. & Mulder, W., 2004. Frequency-domain finite-difference amplitude-preserving migration, *Geophys. J. Int.,* **157**, 975–987.

Reiter, E.C., Toksöz, M.N., Keho, T.H. & Purdy, G.M., 1991. Imaging with deep-water multiples, *Geophysics,* **56**(7), 1081–1086.

Revenaugh, J. & Jordan, T.H., 1991. Mantle layering from ScS reverberations 1. Waveform inversion of zeroth-order reverberations, *J. geophys. Res.,* **96**, 19 749–19 762.

Schuster, G.T., Yu, J., Sheng, J. & Rickett, J., 2004. Interferometric/daylight seismic imaging, *Geophys. J. Int.,* **157**(2), 838–852.

Shan, G. & Biondi, B., 2004. Imaging overturned waves by plane-wave migration in tilted coordinates, *SEG Tech. Prog. Expand. Abstr.,* **23**(1), 969–972.

Shin, C., Jang, S. & Min, D.-J., 2001. Improved amplitude preservation for prestack depth migration by inverse scattering theory, *Geophys. Prospect.,* **49**, 592–606.

Sjöstrand, J. & Grigis, A., 1994. *Microlocal Analysis for Differential Operators: An Introduction,* Cambridge University Press, Cambridge.

Stolk, C.C. & de Hoop, M.V., 2006. Seismic inverse scattering in the downward continuation approach, *Wave Motion,* **43**(7), 579–598.

Stolk, C.C. & de Hoop, M.V., 2007. Curvilinear wave-equation angle transform: caustics, turning rays, absence of kinematic artifact, in *Expanded Abstracts,* pp. 2180–2183, Society of Exploration Geophysicists.

Vasconcelos, I., Snieder, R. & Hornby, B., 2007. Target-oriented interferometry—imaging with internal multiples from subsalt VSP data, *SEG Tech. Prog. Expand. Abstr.,* **26**(1), 3069–3073.

Verschuur, D.J. & Berkhout, A.J., 2007. Velocity model estimation using primaries and surface-related multiples, *SEG Tech. Prog. Expand. Abstr.,* **26**(1), 2837–2841.

Vivas, F.A., Pestana, R.C. & Ursin, B., 2008. Stabilized least-squares imaging condition, *Geophysics,* submitted.

Weglein, A., Gasparotto, F.A., Carvalho, P.M. & Stolt, R.H., 1997. An inverse-scattering series method for attenuating multiples in seismic reflection data, *Geophysics,* **62**, 1975–1989.

Weglein, A. et al., 2003. Inverse scattering series and seismic exploration, *Inverse Problems,* **19**, R27–R83.

Xie, X.-B. & Wu, R.-S., 2006. A depth migration method based on the full-wave reverse-time calculation and local one-way propagation, *SEG Tech. Prog. Expand. Abstr.,* **25**(1), 2333–2337.

Xu, S. & Jin, S., 2006. Wave equation migration of turning waves, *SEG Tech. Prog. Expand. Abstr.,* **25**(1), 2328.

Xu, S. & Jin, S., 2007. An orthogonal one-return wave-equation migration, *SEG Tech. Prog. Expand. Abstr.,* **26**(1), 2325–2329.

Youn, O.K. & Zhou, H., 2001. Depth imaging with multiples, *Geophysics,* **66**(1), 246–255.

Zhang, Y., Xu, S. & Zhang, G., 2006. Imaging complex salt bodies with turning-wave one-way wave equation, *SEG Tech. Prog. Expand. Abstr.,* **25**(1), 2323.